



Implementation of a roughness sublayer parameterization in the Weather Research and Forecasting model (WRF version 3.7.1) and its validation for regional climate simulations

Junhong Lee^{1,2}, Jinkyu Hong¹, Yign Noh¹, Pedro A. Jiménez³

5 ¹Department of Atmospheric Sciences, Yonsei University, Seoul, South Korea

²Max Planck Institute for Meteorology, Bundesstraße 53, 20146 Hamburg, Germany

³Research Application Laboratory, National Center for Atmospheric Research, Boulder, CO, USA

Correspondence to: Jinkyu Hong (jhong@yonsei.ac.kr)

Abstract. The roughness sublayer (RSL) is one compartment of the surface layer (SL) where turbulence deviates from Monin–Obukhov similarity theory. As the computing power increases, model grid sizes approach to the gray zone of turbulence in the energy containing range and the lowest model layer is located within the RLS. In this perspective, the RSL has an important implication in atmospheric modelling research. However, it has not been explicitly simulated in atmospheric mesoscale models. This study incorporates the RSL model proposed by Harman and Finnigan (2007, 2008) into the Jiménez et al. (2012) SL scheme. A high-resolution simulation performed with the Weather Research and Forecasting model (WRF) illustrates the impacts of the RSL parameterization on the wind, air temperature, and rainfall simulation in the atmospheric boundary layer. As the roughness parameters vary with the atmospheric stability and vegetative phenology in the RSL model, our RSL implementation reproduces the observed surface wind, particularly over tall canopies in the winter season by reducing the root mean square error (RMSE) from 3.1 to 1.8 m s⁻¹. Moreover, the improvement is relevant to air temperature (from 2.74 to 2.67 K of RMSE) and precipitation (from 140 to 135 mm month⁻¹ of RMSE), although its impact is not as substantial as that to wind speed. Our findings suggest that the RSL must be properly considered both for better weather and climate simulation and for the application of wind energy and atmospheric dispersion.

1 Introduction

The Planetary boundary layer (PBL) is important for the proper simulation of weather, climate, wind energy application, and air pollution. Turbulence plays a critical role in the spatio–temporal variation of the PBL structure through the turbulent exchanges of momentum, energy, and water between the atmosphere and Earth’s surface. Because turbulent eddies in the PBL are smaller than the typical grid size in mesoscale and global models, their impacts must be properly parameterized for atmospheric models. The surface layer (SL) occupies the lowest 10% of the ABL, where the shear-driven turbulence is dominant. In the SL, Monin–Obukhov similarity theory (MOST), which is a zero-order turbulence closure, provides the relationships between the vertical distribution of wind and scalars and the corresponding fluxes in a given stability condition



30 (Obukhov, 1946; Monin and Obukhov, 1954). The typical numerical weather prediction (NWP) and climate models are applied for the SL parameterization based on MOST to parameterize the subgrid-scale influences of the turbulent eddies in the PBL (e.g., Sellers et al., 1986, 1996).

35 The SL has two parts: inertial sublayer (ISL) and roughness sublayer (RSL). The ISL is the upper part of the SL, where MOST is valid and vertical variation of the turbulent fluxes is negligible. The RSL is the layer near and within the surface roughness elements (e.g., trees and buildings). The turbulent transport in the RSL has a mixing layer analogy, and the atmospheric flow depends on the roughness element properties (Raupach et al., 1996). Accordingly, the flux–gradient relationships in the RSL deviate from the MOST predictions, and the eddy diffusion coefficients are larger than the values in the SL (e.g., Shaw et al., 1988; Kaimal and Finnigan, 1994; Brunet and Irvine, 2000; Finnigan, 2000; Hong et al., 2002; Dupont and Patton, 2012; Shapkalijevski et al., 2016; Zhan et al., 2016; Basu and Lacser, 2017).

40 Traditionally, the RSL has not been explicitly considered in global and mesoscale models because the PBL in the model is coarsely resolved, and the lowest model layer is well above the roughness elements accordingly. As the computing power increases, the regional and global models can be simulated with a finer spatial resolution and the grid size of the NWP model moving toward the gray zone of turbulence (the scales on the order of the energy-containing range of turbulence). Nevertheless, 45 studies on the impact of a fine vertical resolution have not been relatively performed. In this perspective, the RSL has an important implication in atmospheric modelling research. The lowest model layer is typically approximately 30 m high, and its vertical resolution continues to be better; hence, the models have more than one vertical layer in the RSL, which extends to 2–3 times of the canopy height. Furthermore, model outputs are sensitive to the selection of the lowest model level height (Shin et al., 2011), but its relation to the RSL has not yet been clearly investigated. Accordingly, turbulent transport in the RSL must be incorporated particularly in the mesoscale models if the vertical model levels are inside the RSL with an increase in 50 the vertical model resolution.

The RSL function is a popular and simple method of incorporating the effects of the RSL in the observation and model (e.g., Raupach, 1992; Physick and Garratt, 1995; Wenzel et al., 1997; Mölder et al., 1999; Harman and Finnigan, 2007, 2008; de Ridder, 2010; Arnqvist and Bergström, 2015). The RSL function is defined as the observed relationship between the vertical gradient of wind and scalar and their corresponding fluxes in the RSL. Accordingly, simple relationships are appropriate for 55 the land surface model in the climate model and for the mesoscale model (Physick and Garratt, 1995; Sellers et al., 1986, 1996). Despite the importance of the RSL, the Weather and Research Forecasting (WRF) model (Skamarock et al., 2008), which is one of the widely used models in the operation and research fields, does not consider the effects of the RSL, and has not yet been evaluated in the regional weather and climate simulations. Harman and Finnigan (2007, 2008) and Harman (2012) (hereafter, HFs) recently proposed a relatively simpler RSL function that can be used in a wide range of atmospheric models. 60 The RSL function of the HFs is based on a theoretical background and applicable to a wide range of atmospheric stabilities by succinctly satisfying the continuity of the vertical profiles of fluxes, wind, and scalars both at the top of the RSL and at the top of a canopy. The parameterization of HFs has recently been incorporated in a one-dimensional (1D) PBL model and a land surface model (Harman, 2012; Shapkalijevski et al., 2017; Bonan et al., 2018).



Based on the abovementioned background, this study incorporates the RSL parameterization based on the RSL function of the HFs into the WRF model (version 3.7.1). For this purpose, we reformulate the HFs' RSL parameterization to implement it to the SL parameterization in the WRF model and then discuss the impacts of the RSL parameterization on the regional weather and climate simulations in terms of meteorological conditions near the Earth surface. To the best of the authors' knowledge, our study is the first extensive attempt to incorporate RSL parameterization into the WRF model and to validate it for regional climate simulations. Section 2 is a brief discussion of the RSL parameterization of HFs and the implementation procedures into the WRF model. Section 3 explains the experimental and observational descriptions. Section 4 presents the impacts of the RSL parameterization. Section 5 ends the study with the concluding remarks.

2 RSL theory of the HFs

The roughness sublayer parameterization by HFs is adopted herein along with an explanation of the core of the HF model, and the relevant details on this parameterization can be found in Harman and Finnigan (2007, 2008) and Harman (2012). Appendix 75 A lists in alphabetical order the symbols used in this study.

We first define the coordinate alignment for its application to the WRF. The revised MM5 SL scheme in the WRF model defines the vertical origin by the conventional zero-plane displacement height (d_0). The same coordinate system is also applied herein. The vertical coordinates z and \tilde{z} in this coordinate system are defined as the distance from d_0 and from the terrain surface, respectively; therefore, their relation is $z = \tilde{z} - d_0$. Note that a vertical origin in the HFs is at the canopy height (h).
 80 MOST says that a variable (C), such as wind speed (u) and temperature (T), has the logarithmic vertical profile:

$$\frac{k}{C_*} (C(z) - C_0) = \ln\left(\frac{z}{z_0}\right) - \psi_c\left(\frac{z}{L}\right) + \psi_c\left(\frac{z_0}{L}\right), \quad (1)$$

where k is von Kármán constant; C_* is a C scale; C_0 is C at z_0 ; z_0 is the roughness length; ψ_c is the integrated similarity function of C ; and L is the Obukhov length. The C profile based on the RSL function of the HFs is divided into two layers depending on the relative distance between h and the redefined zero-plane displacement height in the HFs ($d_t = h - d_0$): the upper-canopy layer ($z > d_t$), where the influence of additional mixing by the canopy exists, and the lower-canopy layer ($z < d_t$), where 85 the canopy is the direct source and sink for drag and heat. The vertical profile in the upper-canopy layer is described as follows:

$$\frac{k}{C_*} (C(z) - C_0) = \ln\left(\frac{z}{z_0}\right) - \psi_c\left(\frac{z}{L}\right) + \psi_c\left(\frac{z_0}{L}\right) + \int_z^\infty \frac{\phi_c(1-\hat{\phi}_c)}{z'} dz', \quad (2)$$

where ϕ_c is the similarity function of C and $\hat{\phi}_c$ is an RSL function of C . The last term in the right-hand side represents the additional mixing caused by the roughness element due to the coherent canopy turbulence, and can be replaced by $\hat{\psi}_c$, which is an integrated RSL function of C . The vertical profile from the HFs for the RSL deviates from that of MOST because of $\hat{\psi}_c$, thereby adjusting the logarithmic profile. The $\hat{\phi}_c$ is introduced as follows:

$$\hat{\phi}_c = 1 - c_1 \exp\left[-c_2 \frac{\beta}{l_m} z\right]. \quad (3)$$



90 The RSL function, $\hat{\phi}_c$ exponentially converges to zero above the RSL. c_1 and c_2 are then determined from the continuity of $\hat{\phi}_c$ at the canopy top. In the lower canopy layer, C has the following exponential form:

$$C(z) - C_0 = (C_h - C_0) \exp\left(f \frac{z-d_t}{2d_t}\right), \quad (4)$$

The RSL functions vary with atmospheric stability through β ,

$$\beta = \begin{cases} \frac{\beta_N}{\phi_m(z=d_t)} & \frac{L_c}{L} > -0.15 \\ \frac{k}{2\phi_m(z=d_t)} + \frac{\beta_N}{\phi_m(z=d_t)} - \frac{k}{2\phi_m(z=d_t)} \frac{1.5}{1+2\left|\frac{L_c}{L}+0.15\right|} & \frac{L_c}{L} \leq -0.15 \end{cases}, \quad (5)$$

where L_c is a canopy penetration depth defined as:

$$L_c = (c_d a)^{-1} = \frac{4h}{LAf}. \quad (6)$$

where c_d is a drag coefficient at the leaf scale and a is the leaf area density. The parameter d_t and z_0 also depend on the stability 95 because of their dependence on β :

$$d_t = h - d_0 = \frac{l_m}{2\beta} = \beta^2 L_c, \quad (7)$$

$$z_0 = d_t \exp\left[-\frac{k}{\beta}\right] \exp\left[-\psi_m\left(\frac{d_t}{L}\right) + \psi_m\left(\frac{z_0}{L}\right)\right] \exp\left[\int_{d_t}^{\infty} \frac{\phi_m(1-\hat{\phi}_m)}{z'} dz'\right], \quad (8)$$

where ψ_m is the integrated similarity function for the momentum.

3 Incorporation of the roughness sublayer parameterization into the WRF model

The RSL parameterization of the HFs described above is implemented in the Jiménez et al. (2012) revised MM5 surface layer scheme and Noah land surface model in the WRF (hereafter called the Yonsei University surface layer (YSL) scheme) because 100 theoretical consistency between the HFs and PBL parameterization. To incorporate the RSL parameterization, it is necessary to modify the SL scheme and the land surface model as follow (Fig. 1): the first step is to compute the bulk Richardson number at the lowest model layer, Bi_b , by the original equation of Jiménez et al. (2012) [Eq. (9) in their study]:

$$Bi_b = \frac{g}{\theta_a} \frac{\theta_{va} - \theta_{vg}}{[U(z_r)]^2} z_r. \quad (9)$$

The second step is to iteratively calculate the atmospheric stability (z_r/L) as follows with an accuracy of 0.01:

$$\frac{z_r}{L} = Bi_b \frac{\left[\ln\left(\frac{z_r}{z_0}\right) - \psi_m\left(\frac{z_r}{L}\right) + \psi_m\left(\frac{z_0}{L}\right) + \hat{\psi}_m\right]^2}{\left[\ln\left(\frac{\rho c_p k u_*^{n-1} z_r}{c_s} + \frac{z_r}{z_l}\right) - \psi_h\left(\frac{z_r}{L}\right) + \psi_h\left(\frac{z_l}{L}\right) + \hat{\psi}_h\right]}. \quad (10)$$

Equation (10) is different from Eq. (23) of Jiménez et al. (2012) by the RSL functions (i.e., $\hat{\psi}_m$ and $\hat{\psi}_h$). After z_r/L is 105 determined, the third step is to iteratively update d_t and β using Eqs. (5) and (6) with an accuracy of 0.0001 because they are



inter-correlated with each other. Subsequently, z_0 is iteratively achieved with an accuracy of 0.0001 using Eq. (7) at the given z_r/L , β , and d_t . The u profile is determined using Eqs. (2) and (4). Following Jiménez et al. (2012), the profile of a scalar, such as T , is determined by

$$\frac{k}{C_*} (C(z) - C_0) = \ln \left(\frac{\rho c_p k u_*^{n-1} z_r}{c_s} + \frac{z_r}{z_l} \right) - \psi_c \left(\frac{z}{L} \right) + \psi_c \left(\frac{z_0}{L} \right) + \int_z^\infty \frac{\phi_c(1-\hat{\phi}_c)}{z'} dz', \quad (11)$$

for the upper-canopy layer. Equation (4) is used for the lower-canopy layer. Finally, u_* and the aerodynamic conductance (g_a) 110 in the RSL are given to

$$u_* = \frac{ku(z_r)}{\left[\ln \left(\frac{z_r}{z_0} \right) - \psi_m \left(\frac{z_r}{L} \right) + \psi_m \left(\frac{z_0}{L} \right) + \bar{\psi}_m \right]} \text{ and,} \quad (12)$$

$$g_{a1} = \frac{\ln \left(\frac{z_r}{d_t} \right) - \psi_h \left(\frac{z_r}{L} \right) + \psi_h \left(\frac{d_t}{L} \right) + \bar{\psi}_h \left(\beta \frac{z_r}{l_m} \right) - \bar{\psi}_h \left(\beta \frac{d_t}{l_m} \right)}{ku_*},$$

$$g_{a2} = \frac{s_c}{\beta^2 u_h} \left[\exp \left(\beta \frac{d_t - z_l}{l_m} \right) - 1 \right]^{-1}, \quad (13)$$

$$g_{a3} = \frac{\ln \left(\frac{\rho c_p k u_*^{n-1} z_l}{c_s} + 1 \right)}{ku_*} \text{ and}$$

$$g_a = \frac{1}{1/g_{a1} + 1/g_{a2} + 1/g_{a3}}.$$

4 Numerical experimental design

This study evaluated the YSL scheme by making a 1D offline test and a real case simulation. The 1D offline simulation was done to test the YSL scheme performance without feedback to the atmosphere. The two 1D offline simulations are carried out; the YSL, the revised MM5 SL schemes coupled with the Noah land surface model, and the Yonsei University (YSU) PBL 115 scheme (hereafter offCTL and offRSL experiments). Table 1 presents the idealized data for boundary condition. The real case simulation consisted of two experiments: one-month simulation during winter (January 2016) with the original revised MM5 SL scheme and the YSL scheme (hereafter referred to as the rCTL and rRSL experiments). The rCTL and the rRSL employed the same physics package, except for the SL scheme and the land surface model (Lee and Hong, 2016 and references therein). One-way nesting was applied herein in a single-nested domain with a Lambert conformal map projection to East Asia (Fig. 2). 120 A 9 km horizontal resolution domain 2 was then embedded in the 27 km resolution domain 1 with 31 vertical layers. The initial and boundary conditions were produced using the National Center for Environmental Prediction Final Analysis data ($1^\circ \times 1^\circ$).

5 Observation data for the model validation



The model performance was examined against the surface wind speed and the temperature observed at 46 Automated Synoptic
125 Observing System (ASOS) sites in Korea (Fig. 2). Quality control of the data includes gap detection, limit test, step test based
on the standard of the World Meteorological Administration and Korea Meteorological Administration (KMA) (Zahumensky,
2007; Hong et al., 2013). For the model validation of the real case simulation, the different measures of the correlation
coefficients, centered root-mean-square differences (RSMD), and standard deviations of the model (σ_m) normalized by that
130 of the observation (σ_o) are shown in a Taylor diagram (Taylor, 2001). In the Taylor diagram, a point nearer the observation at
a reference point (OBS) can be considered to give a better agreement with the observation. We also provide the root-mean-
square error (RMSE) and the mean bias (MB) with the pattern correlation for the rainfall simulation validation.

6 Results

6.1 Offline simulations

Figure 3 shows the roughness parameters (i.e., z_0 , d_r , and β) as a function of the normalized atmospheric stability (L_c/L) from
135 the offline simulation of the YSL scheme. The offline simulations reproduced the results of Harman and Finnigan (2007, 2008).
The roughness parameters varied with the atmospheric stability, L_c/L , and had peaks at weakly unstable conditions. Note that
the roughness length is constant based on the land cover in the traditional atmospheric model such as the WRF.

Figure 4 indicates that the impacts of the roughness sublayer are also decided by L_c , which is a function of LAI and h (Eq. (6)), thus leading to both diurnal and seasonal variation of canopy roughness. Consequently, the roughness parameters showed
140 daily and seasonal variations. Overall, the roughness length in the YSL was larger than the revised MM5 SL scheme,
particularly in a smaller z/L (i.e., neutral and unstable conditions) and a larger L_c (i.e., small LAI and/or large h). The roughness
length in a stable condition showed relatively smaller changes with z/L and L_c compared to those in the unstable condition.
Our findings suggest that L_c becomes larger in the winter season over tall forest canopies because of the smaller LAI , and
145 higher h , thereby leading to relatively larger differences of z_0 between the YSL scheme and the default WRF scheme. On the
contrary, a similar value of z_0 was observed in summer because of the larger LAI . Note that the revised MM5 SL scheme does
not consider d_r and β .

The RSL function, $\hat{\phi}_c$, introduced by HFs, considers the additional mixing caused by the roughness element. Accordingly,
150 $\hat{\phi}_c$ should asymptotically converge to the MOST profile (i.e., $\hat{\phi}_c \rightarrow 1$) as z increases with the continuous vertical profiles of the
wind and the temperature. The YSL scheme reproduced these properties of $\hat{\phi}_c$ and matched with the observed profiles inside
canopies: the YSL scheme showed exponential profiles under the canopy top and logarithmic profiles above the canopy top
(Fig. 5). The wind speed and the air temperature above the canopy top were smaller than predicted by MOST because $\hat{\phi}_c < 1$
in the offRSL experiments. Notably, the YSL scheme produced wind and temperature below the zero-plane displacement
height, thereby providing additional useful information on the atmospheric dispersion inside the canopy.



The roughness length changes in the YSL scheme eventually produced changes in the surface energy balance with the 155 atmospheric stability (Fig. 6). In the offline simulations based on the conditions in Table 1, the YSL produced a larger z_0 in the unstable and near-neutral conditions, but a smaller z_0 in $z/L > 3$ compared to the offCTL. The aerodynamic conductance (g_a) in the YSL was larger in all the stability conditions even in the stable conditions in which the YSL provided a smaller z_0 because the additional term in Eq. (13), g_{a2} , dominated over the other effects in the g_a calculation. Accordingly, H and λE in the YSL were larger than those in the revised MM5 SL scheme. Our finding implies stronger fluxes from the YSL scheme 160 when the gradient of quantity is the same. However, the impact of the increased g_a was asymmetrical in H and λE depending on the soil moisture content. In this case simulation, an increase in λE was dominant because the wet condition made more partitioning of the available energy into the latent heat flux first in the model. However, in the dry condition (i.e., less soil 165 water content), the YSL produced a larger H without a substantial increase of λE (Fig. S1). A significant increase in λE was found along with a decrease in H in the strong unstable conditions (Fig. 6) because of the wet soil moisture of 0.25 m³ m⁻³ in the offRSL simulation in Table 1. The slight increase in the net radiation was mainly associated with the reduced outgoing 170 longwave radiation caused by the smaller surface temperature in the offRSL.

6.2 Real case simulations

Figure 7 shows the real case simulation of the roughness length, 10 m wind speed (u_{10}), and 2 m air temperature (T_2). We 170 discuss herein the real cases in the winter season because of stronger effect of the roughness sublayer. The results for the summer season can be found in the Supplementary Materials. The roughness length in the rCTL experiment was prescribed from the vegetation data table (i.e., VEGPARM table in the WRF model) and modified by the vegetation fraction (Figs. 2 and 7a).

Overall, the YSL scheme (rRSL experiment) produced 0.2–2.0 m larger z_0 than the default values in the rCTL experiment 175 over the tall canopies, where L_c was large. In contrast, the YSL produced a similar or even slightly smaller z_0 over the short canopies compared to the rCTL experiment. Importantly, the changes of z_0 made direct impacts on the momentum fluxes and thus surface wind speed (Fig. 7b). The typical u_{10} in the rCTL was larger than approximately 3 m s⁻¹, and a much stronger wind (> 6 m s⁻¹) was observed along the mountains, making a positive bias against the observation. Overall, the YSL scheme reproduced the better observed diurnal variation by reducing the positive bias of the wind speed (Table 2, Fig. 8). Over the tall 180 forest canopies, u_{10} in the rRSL was reduced by approximately 30%; however, the region of the smaller wind speed corresponded to the short canopies, where the roughness length increased (Figs. 7a and b). The YSL scheme particularly provided better RMSD and correlation coefficient, but less diurnal variability of wind speed because of a relatively larger reduction of the daytime wind speed (Fig. 8). MB and RMSE decreased from 2.4 m s⁻¹ to 1.0 m s⁻¹ and from 3.1 m s⁻¹ and 1.8 m s⁻¹. The Taylor diagram shows that the overall performance of the YSL is better than the default WRF simulation at all the 46 sites. In the Taylor diagram, the statistics moved toward the observation, except for one site, indicating an overall



185 improvement of 2 m air temperature in the YSL scheme; however, the impact of the RSL was not as large as the wind speed (Table 2, Fig. 9).

Similar to the increases of the aerodynamic conductance in the offline simulations, the YSL in the real case simulation (i.e., the rRSL simulation) simulated a larger g_a , particularly in the forest canopies and mountain regions (Fig. 10a). This larger g_a in the YSL led to the increases of the latent heat fluxes by approximately 20 W m^{-2} , with an eventual reduction of the soil 190 water content (Fig. 11a). The sensible heat fluxes in the rCTL experiments were generally approximately 80 W m^{-2} , except over the snow-covered region where H was approximately 40 W m^{-2} . As described in the offline simulation, the changing sign of H in the rRSL depended on the soil moisture content because evapotranspiration is limited in dry soils at given available energy (Figs. 10b and 11b). Consequently, the available energy ($=H + \lambda E$) increased in the YSL scheme, and a larger λE in the rRSL led to a temperature cooler than that in the rCTL experiment (Fig. 7c).

195 During the winter simulation period, precipitation was observed over an extensive area in the domain, and snow was dominant over the northeastern side of the domain (Figs. 11a and 12). The overall total precipitation in the YSL scheme increased, and the skill score indicated a better simulation of the total amount of precipitation (Table 2, Fig. 12). The pattern correlation of precipitation also increased from 0.972 to 0.978 in the YSL scheme based on 656 rain gauge stations, indicating a better match of the precipitation bands. Despite the increase in λE , precipitation decreased in several regions (Figs. 10b and 200 12b). The differences were not significant in the summer season, and the skill scores in the YSL were similar to the default WRF simulation because our implemented RSL parameterization started to converge to the default WRF in a smaller L_c (i.e., smaller LAI and/or higher h) and strong synoptic influences by the summer heavy rainy period (Table S1, Figs. S2–S6).

7 Summary and conclusion remark

Turbulent fluxes regulate the planetary boundary layer; thus, they are a crucial process for weather, climate, and air pollution 205 simulations. Most of the NWP and climate models are commonly applied for MOST to compute the turbulent fluxes near the Earth's surface. MOST can be, however, only applicable in the inertial sublayers and the roughness sublayer, the important compartment of the SL, has not been properly parameterized in the model. Increasing the computing power enables us to use more vertical layers in the atmospheric models. Accordingly, the RSL must be incorporated into the model properly to simulate the atmospheric processes in the gray zone. This study proposed the YSL scheme, which incorporated the RSL into the WRF 210 model, based on the RSL model proposed by Harman and Finnigan (2007, 2008) and Harman (2012). We also investigated the impacts of the RSL parameterization on the weather and climate simulations. For these purposes, we designed a series of offline simulations with an idealized boundary condition and a real case simulation to evaluate the performance of the YSL scheme against the observation data.

The offline simulation revealed that the YSL scheme successfully reproduced the features observed in various canopies 215 and Harman and Finnigan (2007, 2008). The RSL function, $\hat{\phi}_c$, asymptotically increased to 1, and the vertical gradients of the wind speed and the temperature decreased in the RSL as z increased, thereby deviating from the MOST prediction. Notably,



unlike the typical assignment of the roughness parameter as a constant, the roughness parameters (i.e., z_0 , d_t , and β) are functions of the atmospheric stability (z/L) and L_c . The roughness parameters had a maximum in the weakly unstable condition and in larger L_c (i.e., large h or small LAI). In most conditions, the YSL scheme provided a larger roughness length, thereby
220 producing a wind speed slower than that of the revised MM5 SL scheme. The YSL scheme simulated a colder surface temperature in the unstable conditions.

Meanwhile, the real case simulation showed that the RSL-incorporated WRF produced a larger z_0 than the default WRF. This increase in z_0 and its change with atmospheric stability eventually made substantial impacts on the surface energy balance, wind, and temperature near the ground surface, momentum transfer, and precipitation. First, an increase of z_0 produced larger
225 momentum fluxes and a smaller 10 m wind speed when the YSL scheme was applied, leading to the mitigation of substantial positive bias in the wind speed in the revised MM5 SL scheme. The larger z_0 also made increases in the available energy. This increased available energy is related to the surface cooling caused by the increases in the latent heat fluxes in the wet surface conditions when the RSL parameterization is applied. As a result, these changes in the climate near the ground surface and the
230 surface energy balance regulated precipitation, thereby giving a better simulation of the amount of precipitation and its spatial pattern.

Our results indicate that the RSL parameterization can be a promising option for resolving the typical overestimation of the surface wind speed of the WRF model, particularly in the tall vegetation and low LAI, despite a relatively larger computing time (e.g., Hu et al., 2010, 2013; Shimada and Ohsawa, 2011; Shimada et al., 2012; Wyszogrodzki et al., 2013; Lee and Hong, 2016). The improvement caused by the RSL parameterization is useful in air quality modelling and wind energy estimation by
235 better weather and climate in the planetary boundary layer. A further study is necessary to evaluate the characteristics of the YSL scheme in various cases particularly at gray-zone resolutions.

Code and data availability. The source code of the Weather Research and Forecasting Model (WRF) is available at <http://www2.mmm.ucar.edu/wrf/users/downloads.html>. The source code of the YSL scheme and the modelling output presented in this study are available at Github (https://github.com/Yonsei-EAPL/JunhongLee/blob/master/module_sf_ysl.F).
240 The National Center for Environmental Prediction Final Analysis data that was used as initial and boundary conditions is available at <https://rda.ucar.edu/datasets/ds083.2/>. The observed wind speed, temperature, and precipitation for the model validation can be downloaded at the Korea Meteorological Administration data portal (<https://data.kma.go.kr/cmmn/main.do>).



Appendix A: List of symbols and definitions

Symbols	Definitions
a	Leaf area density
Bi_b	Bulk Richardson number, at the lowest model layer
c_d	Drag coefficient at the leaf level
c_p	Specific heat for air
c_s	Effective heat transfer coefficient for nonturbulent processes (Carlson and Boland, 1978; Jiménez et al., 2012)
C	Variable at z , such as u and T
C_0	C at $z = z_0$
C_h	C at h
C_*	Scale of C
d_0	Conventionally defined zero-plane displacement height
d_t	Redefined zero-plane displacement height in Harman and Finnigan (2007)
f	Parameter related the depth scale of the scalar profile
g	Gravitational acceleration
g_a	Aerodynamic conductance
h	Canopy height
k	von Kármán constant
l_m	Mixing length for momentum
L	Obukhov length
L_c	Canopy penetration depth
LAI	Leaf area index



p	Pressure at z
q	Water vapor mixing ratio at z
SW	Downward shortwave radiation
S_c	Turbulent Schmidt number
S_m	Soil moisture
T	Air temperature at z
T_2	Air temperature at 2 m
T_{sk}	Skin temperature
u	Wind speed at z
u_{10}	Wind speed at 10 m
u_h	Wind speed at h
u_*	Friction velocity
u_*^{n-1}	Previous time step value of u_*
z	Height from d_0
\tilde{z}	Height from terrain surface
z_0	Roughness length
z_l	Viscous sublayer depth =0.001 (Carlson and Boland, 1978; Jiménez et al., 2012)
z_r	Height of the lowest model layer
z_r/L	Atmospheric stability
β	u_*/u_h
θ_a	Potential temperature of the air at z_r
θ_{va}	Virtual potential temperature of the air at z_r



θ_{vg}	Virtual potential temperature of the air at ground
ρ	Density of air
ϕ_c	Similarity function of C
$\hat{\phi}_c$	RSL function of C
ψ_c	Integrated similarity function of C
ψ_h	Integrated similarity function of heat
ψ_m	Integrated similarity function of momentum
$\hat{\psi}_c$	Integrated RSL function of C
$\hat{\psi}_h$	Integrated RSL function of heat
$\hat{\psi}_m$	Integrated RSL function of momentum



Author contribution. JL and JH contributed to the code development for the YSL scheme, data analysis, and manuscript preparation. YN and PAJ contributed to the writing and editing of the paper and data analysis.

Competing interests. The authors declare that they have no conflict of interest.

250 *Acknowledgements.* This publication was supported by the National Research Foundation of Korea grant funded by the Korean government (MSIT) (NRF-2018R1A5A1024958), the Korea Meteorological Administration Research and Development Program under Grant KMI2018-03512, and the Korea Polar Research Institute (KOPRI, PN19081).



References

255 Arnqvist, J. and Bergström, H.: Flux-profile relation with roughness sublayer correction, *Q. J. Roy. Meteor. Soc.*, 141, 1191-1197, 2015.

Barlow, J. and Coceal, O.: A review of urban roughness sublayer turbulence, *Tech. Rep.*, No. 527, 68 pp., 2008.

Basu, S. and Lacser, A.: A Cautionary Note on the Use of Monin-Obukhov Similarity Theory in Very High-Resolution Large-Eddy Simulations, *Bound.-Lay. Meteorol.*, 163, 351-355, 2017.

260 Bonan, G. B., Patton, E. G., Harman, I. N., Oleson, K. W., Finnigan, J. J., Lu, Y., and Burakowski, E. A.: Modeling canopy-induced turbulence in the Earth system: a unified parameterization for turbulent exchange within plant canopies and the roughness sublayer (CLM-ml v0), *Geosci. Model Dev.*, 11, 1467-1496, 2018.

Brunet, Y. and Irvine, M. R.: The control of coherent eddies in vegetation canopies: streamwise structure spacing, canopy shear scale and atmospheric stability, *Bound.-Lay. Meteorol.*, 94, 139-163, 2000.

265 Carlson, T. N. and Boland, F. E.: Analysis of urban-rural canopy using a surface heat flux/temperature model, *Bound.-Lay. Meteorol.*, 17, 998-1013, 1978.

de Ridder, K.: Bulk transfer relations for the roughness sublayer, *Bound.-Lay. Meteorol.*, 134, 257-267, 2010.

Dupont, S. and Patton, E. G.: Momentum and scalar transport within a vegetation canopy following atmospheric stability and seasonal canopy changes: the CHATS experiment, *Atmos. Chem. Phys.*, 12, 5913-5935, 2012.

270 Finnigan, J. J.: Turbulence in plant canopies, *Annu. Rev. Fluid Mech.*, 32, 519-571, 2000.

Harman, I. N.: The role of roughness sublayer dynamics within surface exchange schemes, *Bound.-Lay. Meteorol.*, 142, 1-20, 2012.

Harman, I. N. and Finnigan, J. J.: A simple unified theory for flow in the canopy and roughness sublayer, *Bound.-Lay. Meteorol.*, 123, 339-363, 2007.

275 Harman, I. N. and Finnigan, J. J.: Scalar concentration profiles in the canopy and roughness sublayer, *Bound.-Lay. Meteorol.*, 129, 323-351, 2008.

Hong, J., Kim, J., Miyata, A., and Harazono, Y.: Basic characteristics of canopy turbulence in a homogeneous rice paddy, *J. Geophys. Res.*, 107, ACH-8, 2002.

Hong, J.-W., Hong, J., Lee, S., and Lee, J.: Spatial distribution of urban heat island based on local climate zone of automated weather station in Seoul metropolitan area, 23, 1-12, 2013 (In Korean with English abstract)

280 Hu, X. M., Nielsen-Gammon, J. W., and Zhang, F.: Evaluation of three planetary boundary layer schemes in the WRF model, *J. Appl. Meteorol. Clim.*, 49, 1831-1844, 2010.

Hu, X. M., Klein, P. M., and Xue, M.: Evaluation of the updated YSU planetary boundary layer scheme within WRF for wind resource and air quality assessments, *J. Geophys. Res.*, 118, 10-490, 2013.

285 Jiménez, P. A., Dudhia, J., González-Rouco, J. F., Navarro, J., Montávez, J. P., and García-Bustamante, E.: A revised scheme for the WRF surface layer formulation, *Mon. Weather Rev.*, 140, 898-918, 2012.



Kaimal, J. C., and Finnigan, J. J.: Atmospheric boundary layer flows: their structure and measurement, Oxford University Press, United Kingdom, 1994.

Lee, J. and Hong, J.: Implementation of spaceborne lidar-retrieved canopy height in the WRF model, *J. Geophys. Res.*, 121, 6863–6876, 2016.

Mölder, M., Grelle, A., Lindroth, A., and Halldin, S.: Flux-profile relationships over a boreal forest—roughness sublayer corrections, *Agr. Forest Meteorol.*, 98, 645-658, 1999.

Monin, A. S. and Obukhov, A. M. F.: Basic laws of turbulent mixing in the surface layer of the atmosphere, *Contributions of the Geophysical of the Slovak Academy of Sciences*, 151, 163-187, 1954.

Obukhov, A. M.: Turbulence in an atmosphere with a nonuniform temperature, *Trudy Inst. Theor. Geofiz. AN SSSR*, 1, 95–115, 1946.

Physick, W. L. and Garratt, J. R.: Incorporation of a high-roughness lower boundary into a mesoscale model for studies of dry deposition over complex terrain, *Bound.-Lay. Meteorol.*, 74, 55-71, 1995.

Raupach, M.: Drag and drag partition on rough surfaces, *Bound.-Lay. Meteorol.*, 60, 375-395, 1992.

Raupach, M., Finnigan, J. J., and Brunet, Y.: Coherent eddies and turbulence in vegetation canopies: the mixing-layer analogy, Springer, Netherlands, 1996.

Sellers, P. J., Mintz, Y. C. S. Y., Sud, Y. E. A., and Dalcher, A.: A simple biosphere model (SiB) for use within general circulation models, *J. Atmos. Sci.*, 43, 505-531, 1986.

Sellers, P. J., Randall, D. A., Collatz, G. J., Berry, J. A., Field, C. B., Dazlich, D. A., Zhang, C., Collelo, G. D., and Bounoua, L.: A revised land surface parameterization (SiB2) for atmospheric GCMs. Part I: Model formulation, *J. Climate*, 9, 676-705, 1996.

Shapkalijevski, M. M., Moene, A. F., Ouwersloot, H. G., Patton, E. G., and Vilà-Guerau de Arellano, J.: Influence of Canopy Seasonal Changes on Turbulence Parameterization within the Roughness Sublayer over an Orchard Canopy, *J. Appl. Meteorol. Clim.*, 55, 1391-1407, 2016.

Shapkalijevski, M. M., Ouwersloot, H. G., Moene, A. F., and Arrellano, J. V. G. D.: Integrating canopy and large-scale effects in the convective boundary-layer dynamics during the CHATS experiment, *Atmos. Chem. Phys.*, 17, 1623-1640, 2017.

Shaw, R. H., Den Hartog, G., and Neumann, H. H.: Influence of foliar density and thermal stability on profiles of Reynolds stress and turbulence intensity in a deciduous forest, *Bound.-Lay. Meteorol.*, 45, 391-409, 1988.

Shimada, S. and Ohsawa, T.: Accuracy and characteristics of offshore wind speeds simulated by WRF, *Sola*, 7, 21-24, 2011.

Shimada, S., Ohsawa, T., Chikaoka, S., and Kozai, K.: Accuracy of the wind speed profile in the lower PBL as simulated by the WRF model, *Sola*, 7, 109-112, 2011.

Shin, H. H., Hong, S. Y., and Dudhia, J.: Impacts of the lowest model level height on the performance of planetary boundary layer parameterizations, *Mon. Weather Rev.*, 140, 664-682, 2012.

Skamarock, W. C. and Coauthors: A description of the Advanced Research WRF version 3, *Tech. Rep., Note NCAR/TN-4751STR*, 113 pp., doi: 10.5065/D68S4MVH, 2008.



Taylor, K. E.: Summarizing multiple aspects of model performance in a single diagram, *J. Geophys. Res.*, 106, 7183-7192, 2001.

Wenzel, A., Kalthoff, N., and Horlacher, V.: On the profiles of wind velocity in the roughness sublayer above a coniferous forest, *Bound.-Lay. Meteorol.*, 84, 219-230, 1997.

325 Wyszogrodzki, A. A., Liu, Y., Jacobs, N., Childs, P., Zhang, Y., Roux, G., and Warner, T. T.: Analysis of the surface temperature and wind forecast errors of the NCAR-AirDat operational CONUS 4-km WRF forecasting system, *Meteorol. Atmos. Phys.*, 122, 125-143, 2013.

Zhan, E., Dias, N. L., Araújo, A., Sá, L. D. A., Sörgel, M., Trebs, I., Wolff, S., and Manzi, A.: Scalar turbulent behavior in the roughness sublayer of an Amazonian forest, *Atmos. Chem. Phys.*, 16, 11349-11366, 2016.

330



Table 1. Idealized boundary condition for the one-dimensional offline simulation.

Variable	Value	Variable	Value
h	18 m	S_m	$0.25 \text{ m}^3 \text{ m}^{-3}$
LAI	$4 \text{ m}^2 \text{ m}^{-2}$	$T(z_r)$	300 K
Land-use category	Mixed forest	T_{sk}	303 K
L_c	18 m	$u(z_r)$	3 m s^{-1}
$p(z_r)$	1000 hPa	u_*	0.5 m s^{-1}
$q(z_r)$	$9.3 \cdot 10 \text{ kg kg}^{-3}$	z/L	-10–10
SW	800 W m^{-2}	z_0	0.25 m



Table 2. Statistics of the 10 m wind speed, 2 m temperature, and rain rate. The top statistics are presented in bold.

	rCTL	rRSL
10 m wind speed		
Mean bias (m s ⁻¹)	2.4	1.0
Root-mean-square error (m s ⁻¹)	3.1	1.8
2 m temperature		
Mean bias (K)	-0.92	-1.16
Root-mean-square error (K)	2.74	2.67
Rain rate		
Mean bias (mm h ⁻¹)	-0.018	-0.018
Root-mean-square error (mm h ⁻¹)	0.194	0.187
Pattern correlation	0.972	0.978



Input: $\theta(z_r)$, θ_{skin} , $U(z_r)$, z_r
Initial: z_r/L , z_0 , d_t , and β

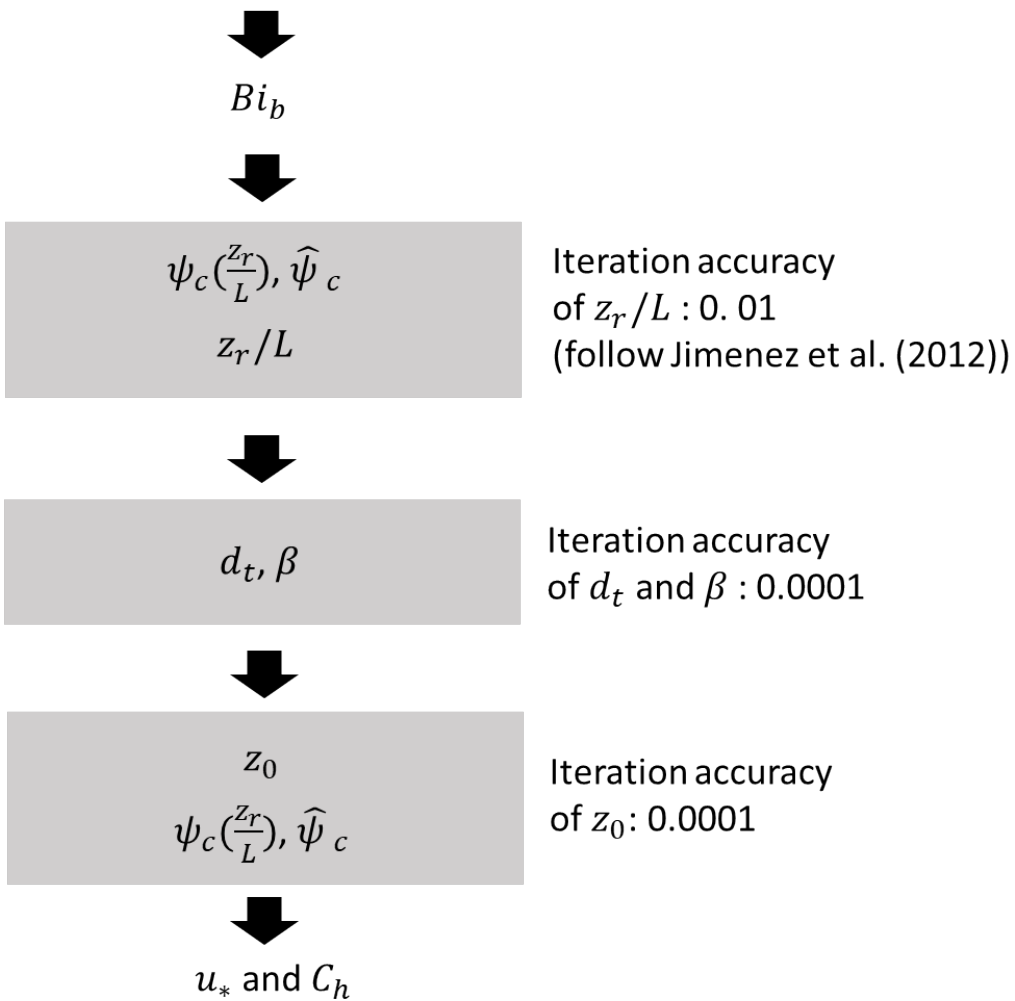
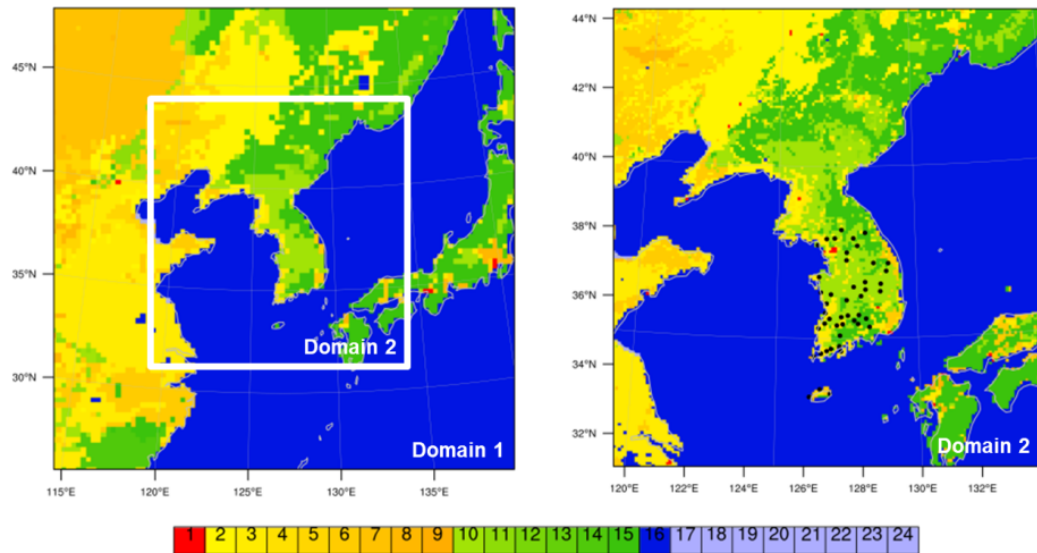
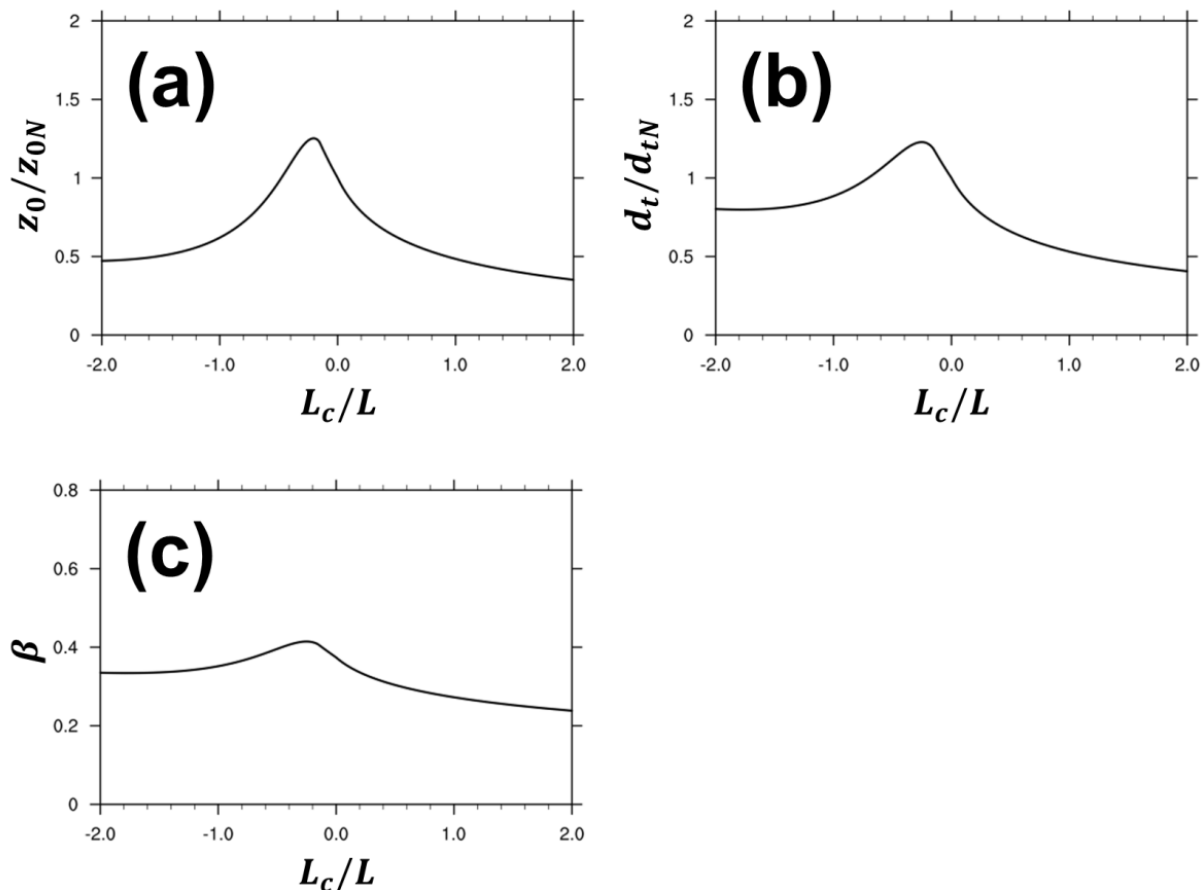


Figure 1: Flow diagram of the RSL parameterization. The gray boxes indicate the iteration module.



1: urban, 2: dry cropland, 3: irrigated cropland, 4: mixed cropland, 5: cropland+grassland,
6: cropland+grassland, 7: grassland, 8: shrubland, 9: shrubland+grassland,
10: savana; 11: Deciduous broadleaf, 12: Deciduous needleleaf, 13: Evergreen,
14: Evergreen needleleaf, 15: mixed forest, 16: water, 17: Herbaceous wetland, 18: Wooded wetland,
19: Barren/sparingly vegetated, 20~23: tundra, 24: snow/ice

340 **Figure 2. Domains and land-use category (USGS) of the real case simulation. Black circles denote the automatic synoptic observing system in Korea used for the model validation.**



345 **Figure 3.** Roughness length (a), displacement height (b), and β (c) normalized by its values in a neutral condition at a given normalized stability (L_c/L) from the offline simulation with the YSL scheme.

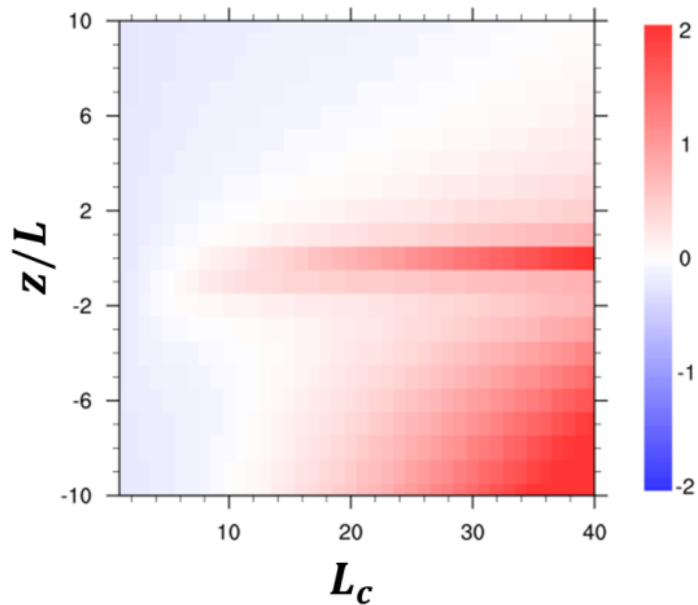


Figure 4. Roughness length difference (m) between offCTL and offRSL (offRSL – offCTL) at given atmospheric stability (z/L) and penetration depth (L_c).

350

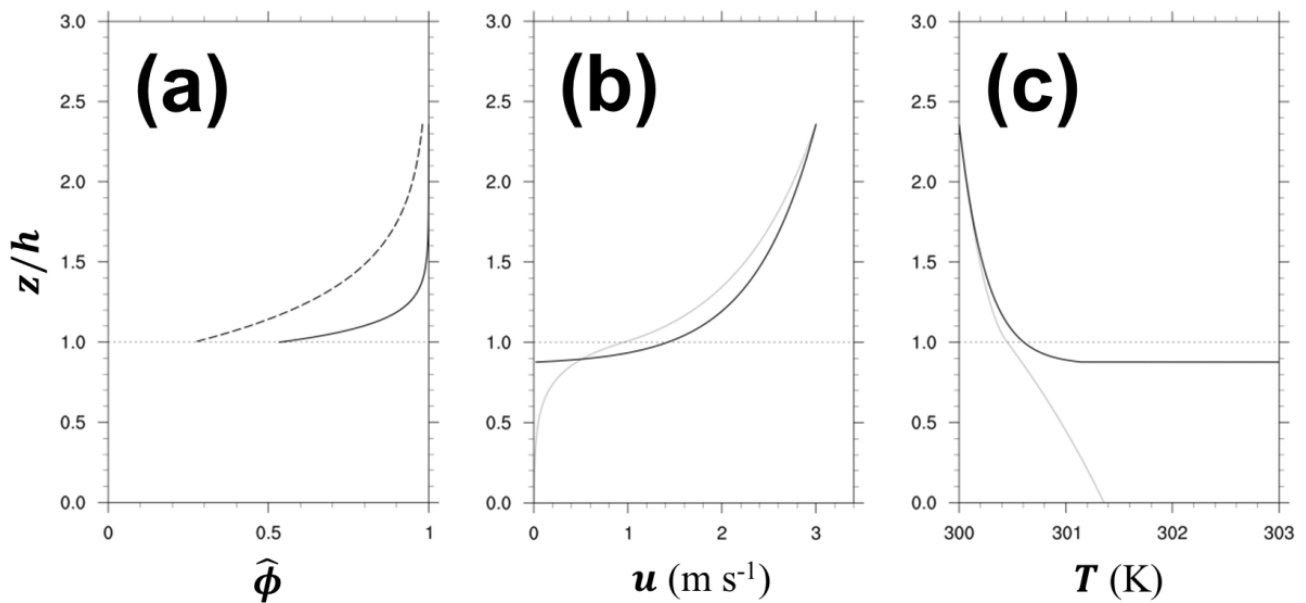


Figure 5. (a) Profiles of the RSL function for momentum ($\hat{\phi}_m$, solid line) and heat ($\hat{\phi}_h$, dashed line), (b) wind speed (m s^{-1}), and (c) temperature (K) at a neutral condition from offCTL (black) and offRSL (gray). The height (z) is normalized by the canopy height (h).

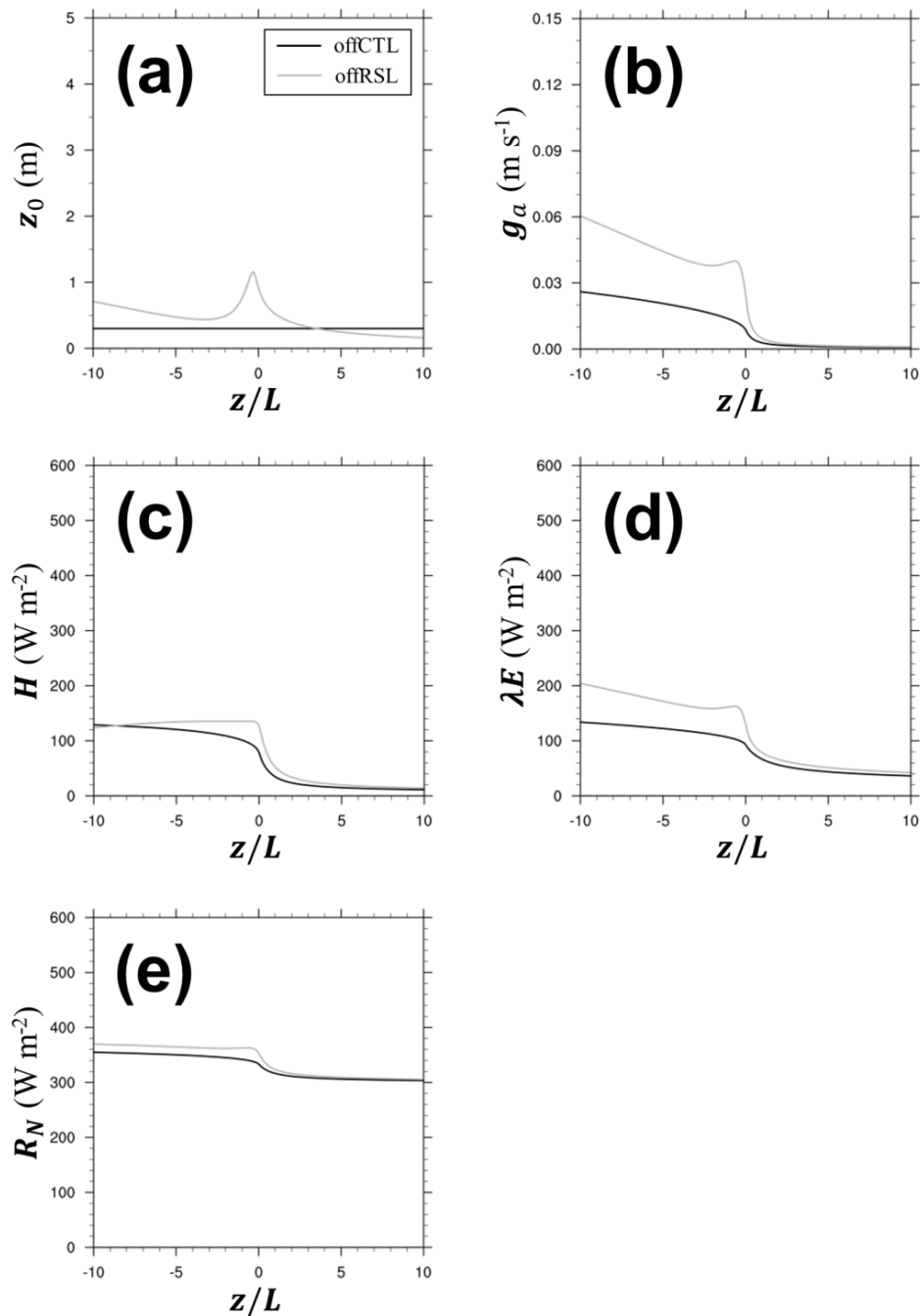


Figure 6. (a) Roughness length (m), (b) aerodynamic conductance (m s^{-1}), (c) sensible heat flux (W m^{-2}), (d) latent heat flux (W m^{-2}), and (e) net radiation (W m^{-2}) at a given atmospheric stability (z/L). The black lines denote offCTL, while the gray lines denote offRSL

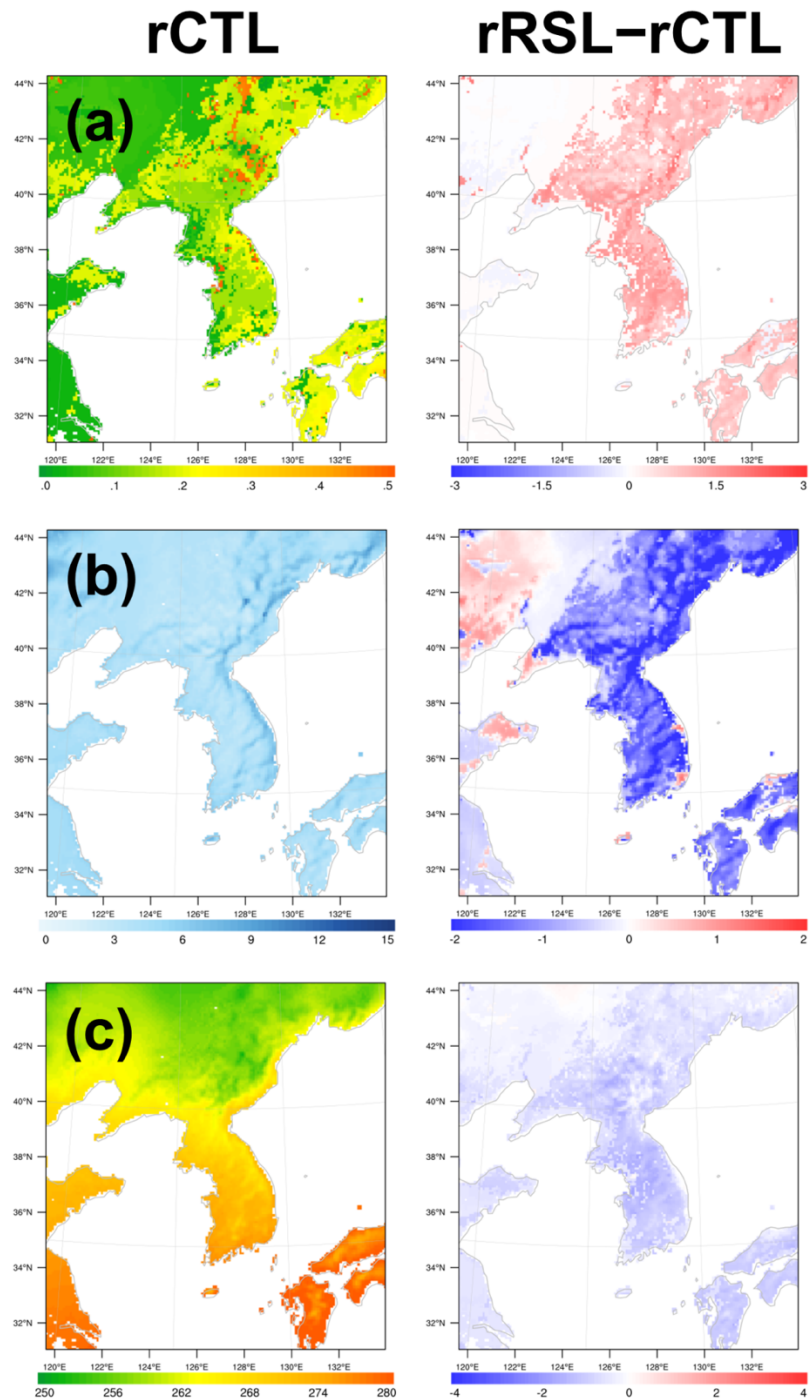
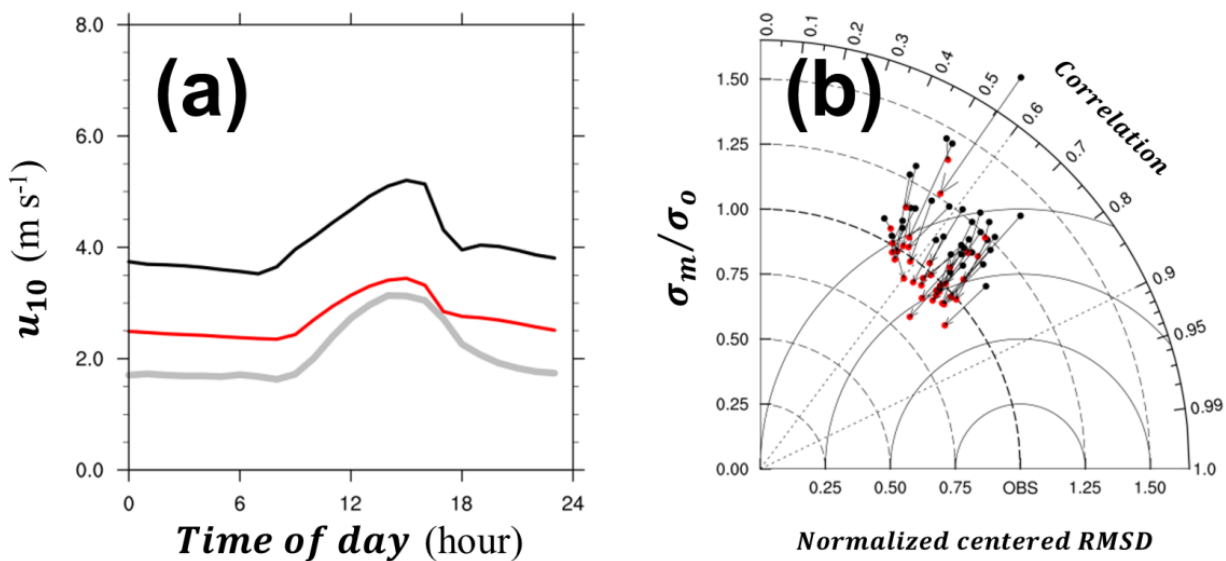


Figure 7. (a) Roughness length (m), (b) 10 m wind speed (m s^{-1}), and (c) daytime 2 m temperature (K) of the (left) rCTL experiment and (right) the difference (rRSL – rCTL). The results are averaged over a period of one month and masked out over the ocean.



365 **Figure 8.** (a) One month mean diurnal variation of 10 m wind speed and (b) the Taylor diagram showing the correlation coefficient, normalized centered root-mean-square differences (RMSD), and standard deviations of the models (σ_m) normalized by that of observation (σ_o) from observation (gray), rCTL experiment (black), and rRSL experiment (red). The vectors indicate the changes of the statistics from rCTL to rRSL. The arrows indicate those from rCTL to rRSL. Every vector shows the movement toward the observation, thereby suggesting the model improvement.

370

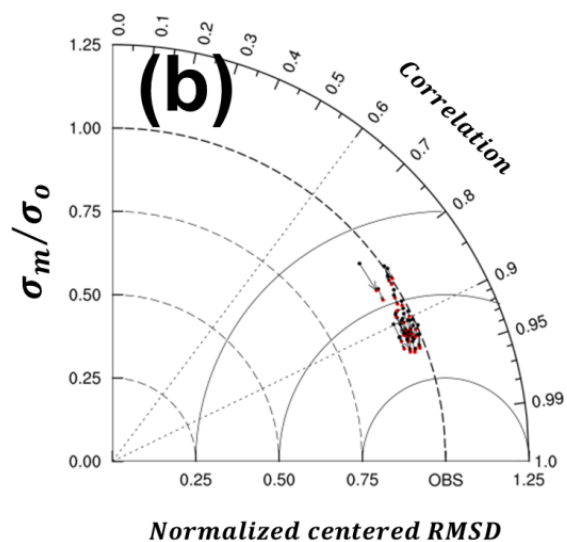
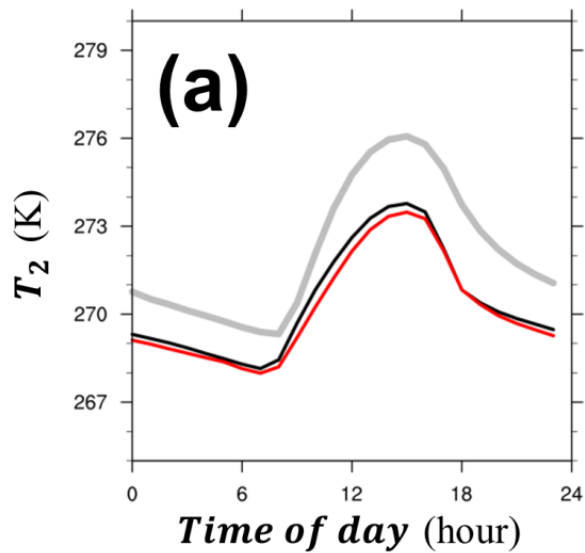
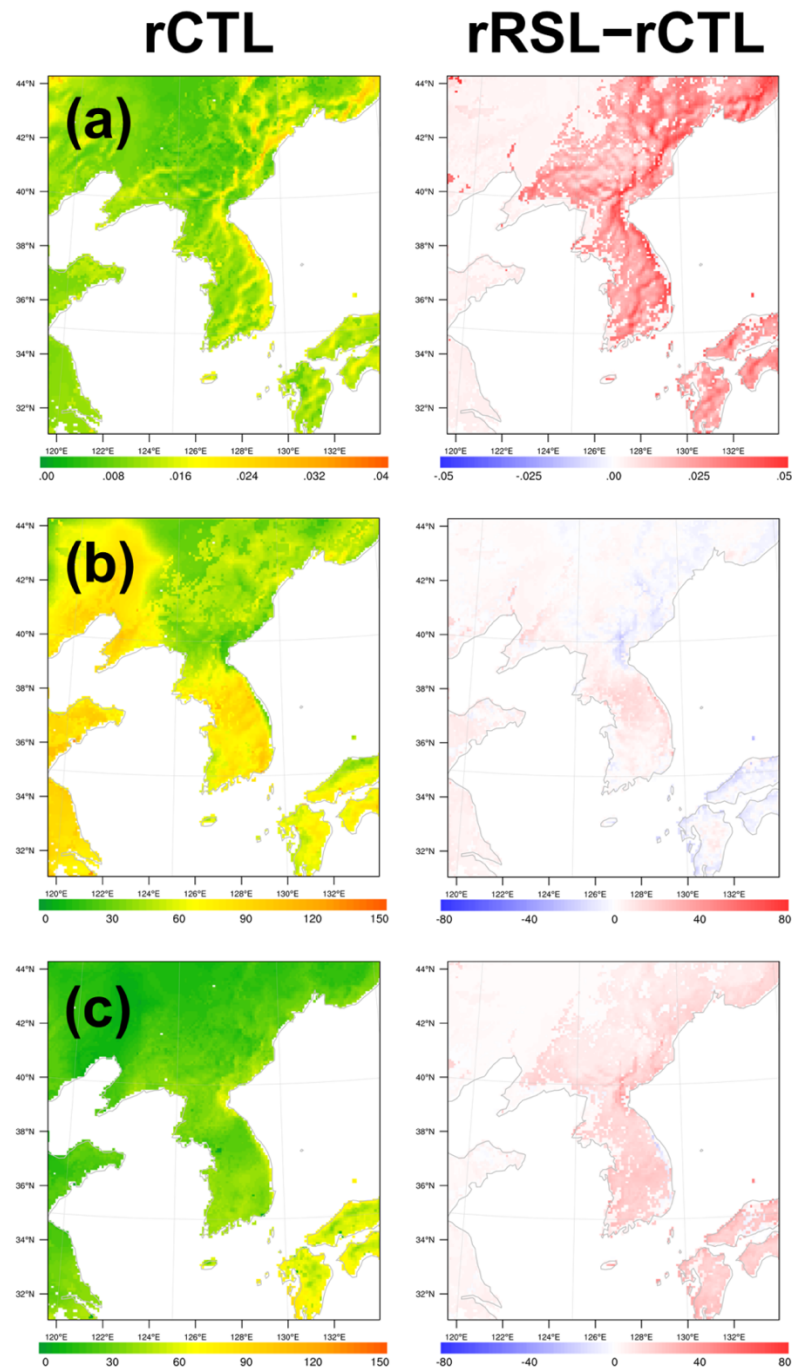
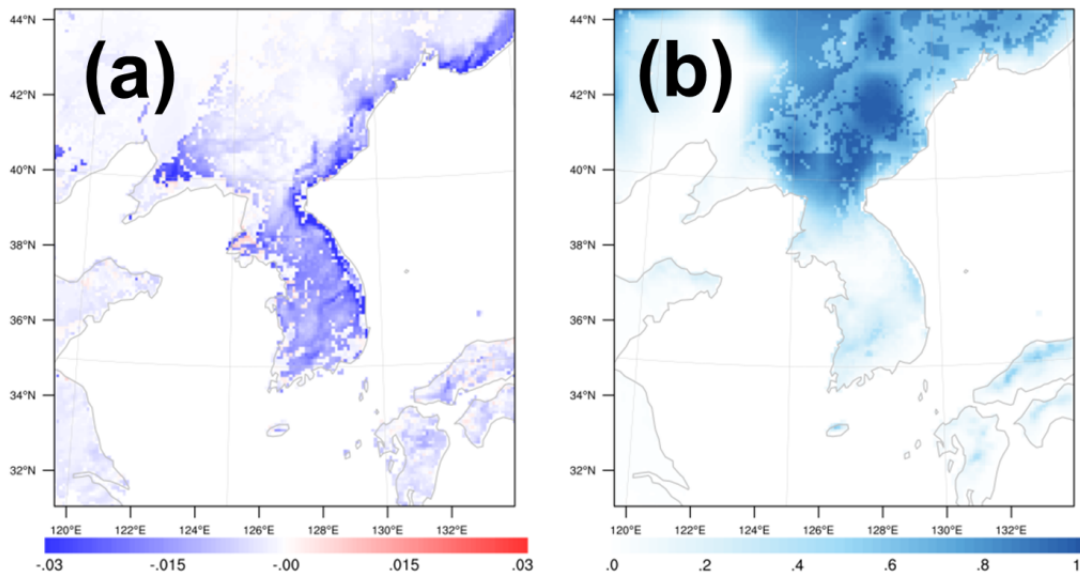


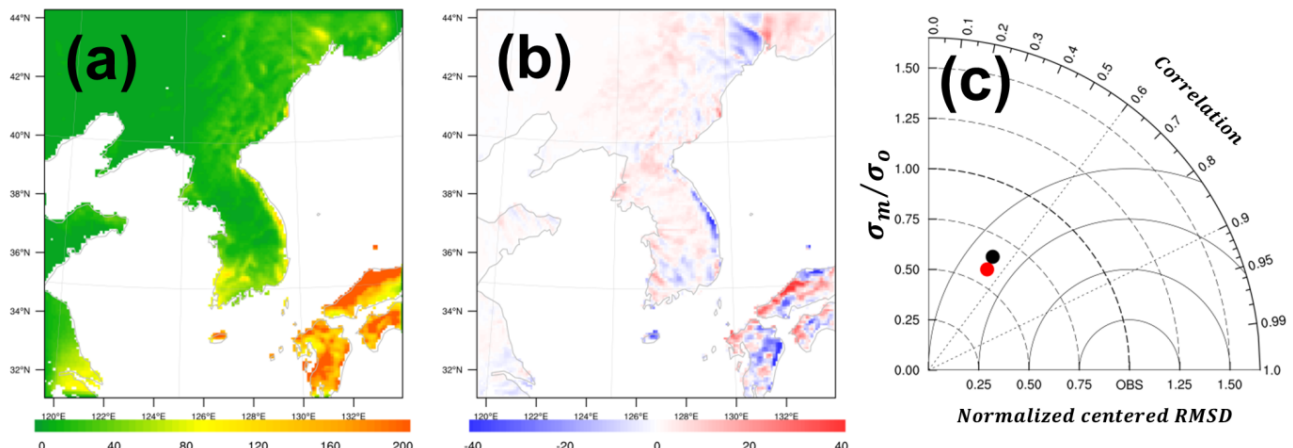
Figure 9. Same as in Fig. 8, but for the 2 m temperature.



375 **Figure 10.** (a) Aerodynamic conductance (m s^{-1}), (b) daytime sensible heat flux (W m^{-2}), and (c) daytime latent heat flux (W m^{-2}) of the (left) rCTL experiment and (right) the difference (rRSL – rCTL). The results are averaged over a period of one month and masked out over the ocean.



380 **Figure 11. (a) Difference of the soil moisture ($\text{m}^3 \text{ m}^{-3}$) ($\text{rRSL} - \text{rCTL}$) and (b) snow cover (%) of rCTL. The results are averaged
over a period of one month and masked out over the ocean.**



385 Figure 12. (a) One month accumulated precipitation of the rCTL experiment (mm) and (b) difference (rRSL – rCTL). (c) Taylor
diagram showing the correlation coefficient, normalized centered root-mean-square difference (RMSD), and the standard
deviations of models (σ_m) normalized by that of the observation (σ_o) and from the rain rate (mm h^{-1}) of the rCTL experiment (black)
and the rRSL experiment (red) during one month at 656 rain gauges.